Optical and Thermal Effects of a Species-Mismatched Supersonic Mixing Layer Formed Over a Cooled Optical Window

Aaron Fassler*, Sergey Leonov† and Stanislav Gordeyev‡

University of Notre Dame, Notre Dame, IN 46556

July 31, 2024

Abstract

The aero-optical distortions caused by supersonic mixing layers over a flat optical window are relevant to the performance of hypersonic vehicles. Such mixing layers are typically temperature-mismatched and gas species-mismatched due to a need to efficiently cool the optical window. To investigate the effect of the mismatched properties across the mixing layer created by blowing a cool gas over a flat window, optical measurements of an M=2 freestream air flow with a cooling two-dimensional gas jet were taken using time-resolved Shack-Hartmann WFS and Schlieren photography. To complement the optical measurements, other non-intrusive techniques, specifically acetone-based PLIF and spatially-resolved infrared thermography techniques were implemented to extract relevant fluidic properties of the mixing layer. The cooling jet gas species were air, helium and carbon dioxide (CO2). To create the temperature mismatch, the total temperature of the freestream flow was varied from 295K to 750K, while the total temperature of the cooling jet was kept constant at 295K. Results of this experimental work will be presented and discussed. Based on experimental input, a scaling method proposed in previous work was implemented in order to predict aero-optical distortions, using the mixing-dominant assumption previously applied to the helium-air and air-CO2 case.

1. INTRODUCTION

Development of hypersonic vehicles is a basis for ongoing aero-optics research. In the high-temperature conditions of hypersonic flow, optical windows will become opaque and therefore useless. However, by recessing the optical window and blowing cold gas across the window, the temperature can be regulated [11]. The result, however, is a mixing layer with a very high M_1 and $T_{0,1}$ and the potential for extreme gradients of density, velocity, and temperature. This flow would be expected to produce large aero-optical effects, degrading the performance of the targeting, computing, or directed energy system. Spencer and Moore (1992) predicted that the effects of beam jitter, blur, and attenuation caused by the mixing layer would comprise approximately 90% of the aero-optical effects of the flow over a hypersonic interceptor missile, as shown in Fig. [16].

To investigate the effect of the mismatched properties across the mixing layer created by blowing a cool gas over a flat window, optical measurements of an $M = 2$ freestream air flow with a cooling two-dimensional gas jet were taken using Shack-Hartmann WFS and Schlieren photography techniques. The cooling jet gas properties were air at $M \approx 0.54$, helium at $M \approx 0.30$, and carbon dioxide (CO_2) at $M \approx 0.65$. Total temperature of the freestream flow was varied from $295K$ to $750K$, while the total temperature of the cooling jet was kept constant at $295K$. Parameters of the mixing flow were examined using optical velocity methods.

It is desired to minimize heat flux into the optical window, to ensure the window does not subsequently become optically opaque. To investigate heat flux, Infrared (IR) Thermography measurements were performed, replacing the optical window from the previous optical measurements with a more thermally emissive anodized coating. IR Thermography measurements produced time-dependent surface maps of temperature, from which

*Graduate Research Assistant, Aerospace and Mechanical Engineering Department. AIAA Student member.
†Research Professor, Aerospace and Mechanical Engineering Department. AIAA Associate Fellow.
‡Associate Professor, Aerospace and Mechanical Engineering Department. AIAA Associate Fellow.

Unconventional Imaging, Sensing, and Adaptive Optics 2024, edited by Jean J. Dolne, Santasri R. Bose-Pillai, Matthew Kalensky, Proc. of SPIE Vol. 13149, 131490B
© 2024 SPIE · 0277-786X · doi: 10.1117/12.3027742

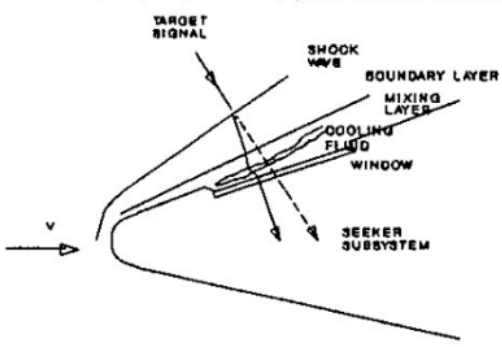

SOURCE OF AO EFFECT	% OF TOTAL EFFECT BSE	JITTER	BLUR	ATTEN.
BOW SHOCK	50%	<1%	.5%	.5%
BOUNDARY LAYER	<1%	10%	5%	10%
COOLANT LAYER	20%	<1%	<1%	<1%
MIXING LAYER	15%	90%	90%	90%
WINDOW	10%	<1%	5%	<1%

Figure 1: Schematic of flow over the tip of a hypersonic missile with an optical window, with a table of aero-optical contributions from each feature [16].

one-dimensional heat flux may be calculated via an adaptation of the QCALC subroutine [2] [10]. From this data, the balance between the minimization of optical effects and the minimization of heat flux may be examined.

Planar Laser-Induced FLuorescense (PLIF) measurements were taken in the upstream-downstream and wall-normal plane. Qualitative and quantitative data from PLIF measurements provide profiles of the molar fractions of the two species in the mixing layer, which may further provide profiles of relevant properties, particularly density. This measurement technique is an important step in taking the modeling approach away from a bulk-flow assumption and towards an approach using exact profiles in the beam propagation direction.

Two new scaling methods for optical effects are examined. One scaling method assumes that the large vortical structures with related pressure drops are responsible for optical distortions. The second method is based on a pure mixing mechanism. It was demonstrated that distortions for air-air case were mostly pressure-dominant, while the helium-air and CO_2-air cases were predominantly mixing-dominant. This mixing-dominant approach is also examined for the air-air case. Results are compared to simulations modeled after experimental conditions by colleagues at New Mexico State University and found to be in good agreement both qualitatively and quantitatively [3].

2. EXPERIMENTAL SETUP

All experiments were performed in Notre Dame's SBR-50 tunnel in White Field Laboratories, which may be described as being configured as a combination of blowdown and Ludwieg tube schemes. The tunnel is designed for either $M = 2$ or $M = 4$ flow. For these experiments, $M = 2$ flow was selected. The driver section can be pressurized to stagnation pressures between 1 and 4 bar. A stagnation pressure of $P_0 = 2.6\ bar = 2.6 \times 10^5 Pa$ was selected for all experiments. The driver section can also be heated to stagnation temperatures between 300K and 775K. Typical steady-state flow duration is 0.5-2 s [1]. An overview of the SBR-50 facility can be found in Fig. 2.

2.1 Test Section

The test section insert, schematically shown in Fig. 3, is comprised of a larger aluminum frame, a 3-D printed plastic nozzle, and an aluminum cover plate with a thickness of 1 mm. These parts are secured to one another

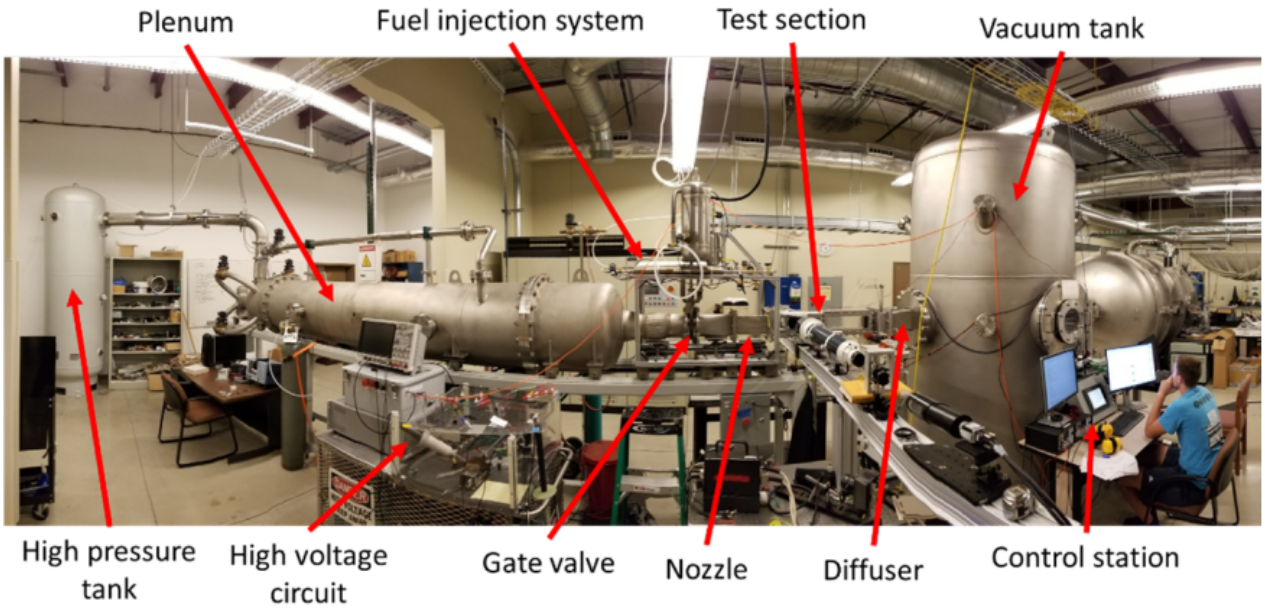

Figure 2: View of SBR-50 facility with components labeled [1].

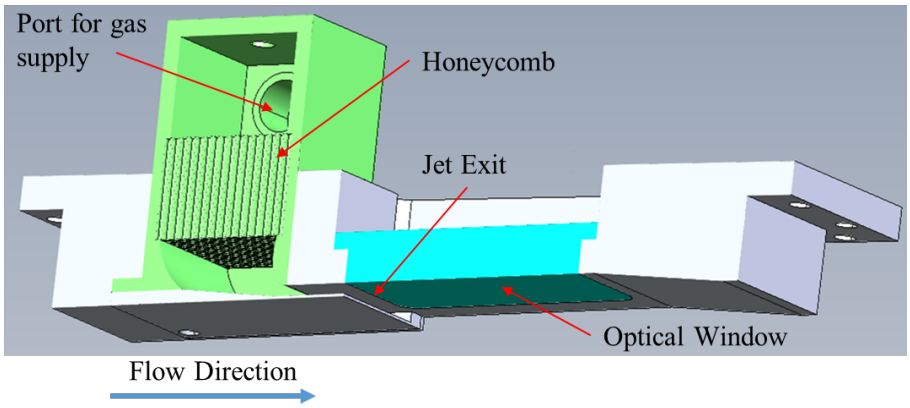

Figure 3: Diagram of a test section insert with a vertical cross-cut with components and features labeled.

with screws. On the far upstream and far downstream edges, the test section insert conforms to the rest of the test section. In the center, the section is recessed. In addition, the test section insert contains an optical window set downstream of the nozzle exit. The depth of the step is 5 mm and the span of the insert is 76 mm, the same as the test section span. Just upstream of the step, the height of the test section is approximately 77 mm. The optical window is set directly downstream of the exit of the nozzle, and has a length of 100 mm and a width of 50 mm. The overall length of the cavity is 108 mm. The nozzle exit has a cross-sectional area of approximately 289 mm^2. Both spanwise faces of the nozzle contain 1/2 NPT threaded holes for gas supply from a compressed air tank. In all experiments, the gas supply comprised of air pressurized to 9 $psig$ in order to match the static pressure between the exit jet in the freestream. In the midsection of the nozzle, a "honeycomb" mesh pattern is set in order to reduce turbulence from the gas supply. The nozzle section area is at a minimum at its exit, and therefore is designed to have an exit Mach number of 1. The upper face of the nozzle contains a 1/8 NPT threaded hole for a pressure probe to monitor the pressure of the gas supply.

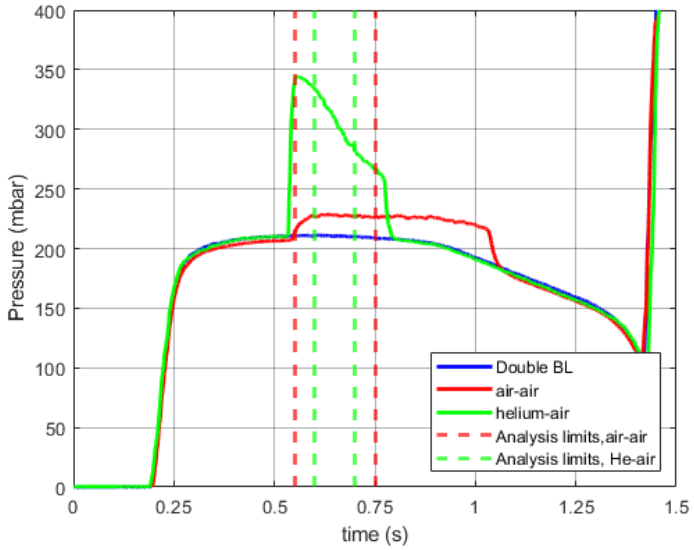

Figure 4: Time-dependent static pressure values from a pressure probe set downstream of the test section. Vertical lines indicate the time intervals used for the wavefront analysis.

2.2 Schlieren and Shack-Hartmann WFS

For all Schlieren and Shack-Hartmann WFS tests, the gas supply was opened 500 ms after the tunnel flow startup. This is because after 500 ms, the tunnel flow is fully developed and tunnel conditions become mostly steady until approximately 1 s, as demostrated by the pressure trace in Fig. 4. For air and CO_2 as cooling gases, the gas supply was closed 1000 ms after the tunnel flow startup. In case of helium as a cooling gas, the gas supply was closed 750 ms after the tunnel flow startup, in order to conserve valuable test gas.

Stagnation temperature in the wind tunnel was first kept at ambient condition of 295K, then heated between 350K and 750K in steps of 100K. Tests with these conditions were repeated for both the air-air and the helium-air cases. A matrix of the test conditions can be found in Table 1.

Table 1: Test freestream conditions.

Run #	1	2	3	4	5	6
T_0	295 K	350 K	450 K	550 K	650 K	750 K
U_∞	510 m/s	560 m/s	630 m/s	700 m/s	760 m/s	820 m/s

A schematic of the optical measurements is presented in Fig. 5. As mentioned before, a large transparent flat optical window was flush-mounted into the floor of the cavity immediately downstream of the cooling jet nozzle. Another optical window of the same size was installed on the opposite (bottom) side of the tunnel test section to provide optical access in the wall-normal direction. A collimated laser beam 50 mm in diameter was forwarded into the test section in the wall-normal direction. The edge of the beam was placed 15 mm downstream from the nozzle exit plane. After being reflected from a flat return mirror outside of the test section, the beam was sent back to the optical table exactly along the same path it came into, thus doubling the optical signal. The outgoing beam was forwarded into a high-speed Shack-Hartmann wavefront sensor (WFS) to measure time-resolved spatial wavefronts caused by the turbulent flow in the cavity. The high-speed camera used in all tests was a Phantom v2512 camera. The lenslet array placed on the camera lens has a pitch of 0.3 mm and a focal length of 38.2 mm. Tests were performed at a sampling frequency of 75 kHz. From this data, both deflection angles and wavefront data were obtained. A labelled picture of the Shack-Hartmann Wavefront Sensor setup is shown in Fig. 6.

To compliment the wall-normal optical measurements, a time-resolved Schlieren system in the spanwise-direction was used to qualitatively evaluate the flow topology of the incoming boundary layer and the mixing layer. Schlieren imaging was performed in the spanwise direction in order to qualitatively characterize the flow and to

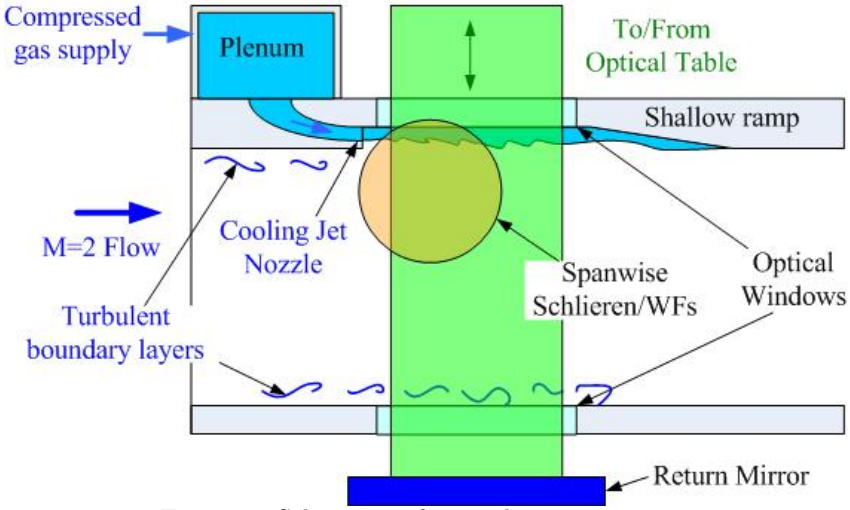

Figure 5: Schematic of optical measurements.

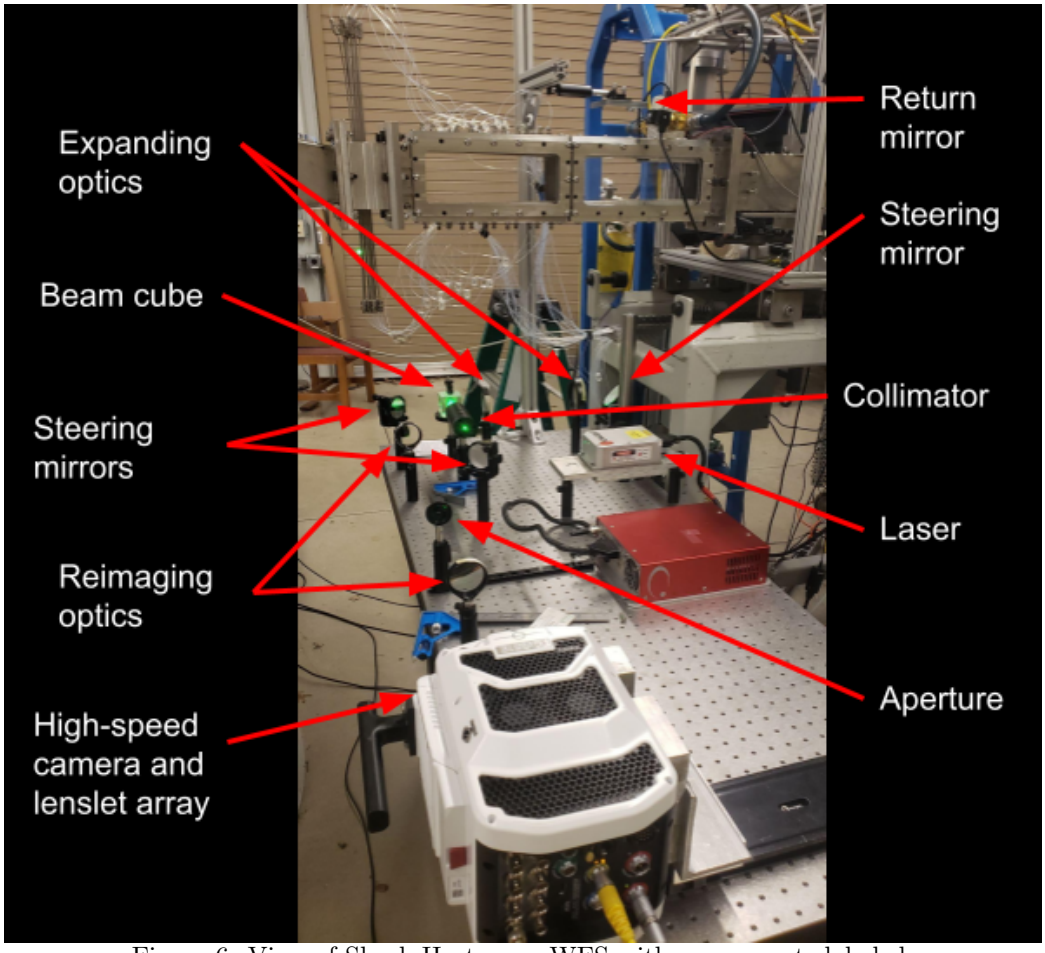

Figure 6: View of Shack-Hartmann WFS with components labeled.

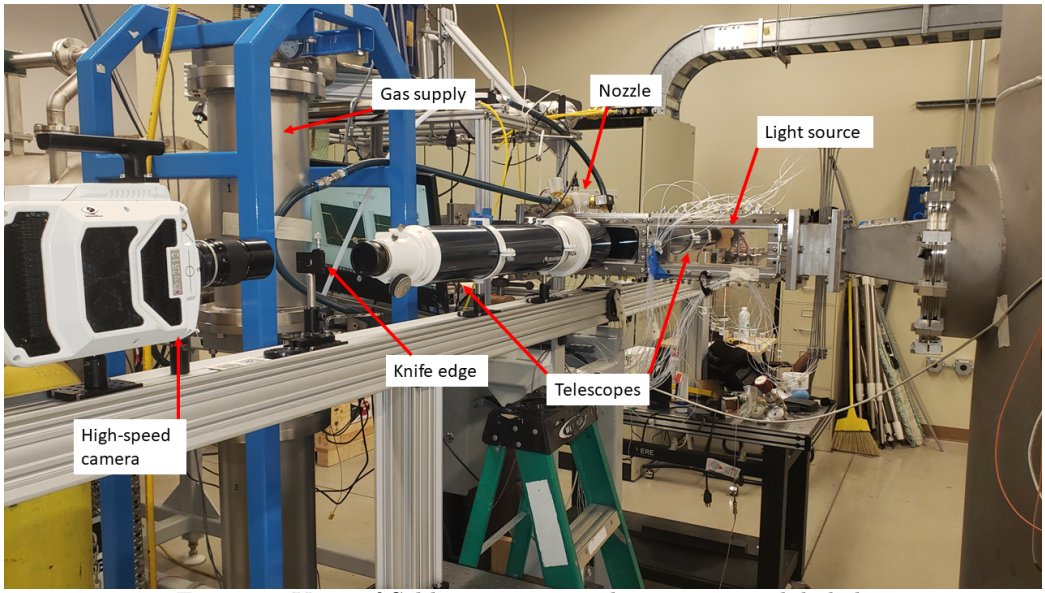

Figure 7: View of Schlieren setup with components labeled.

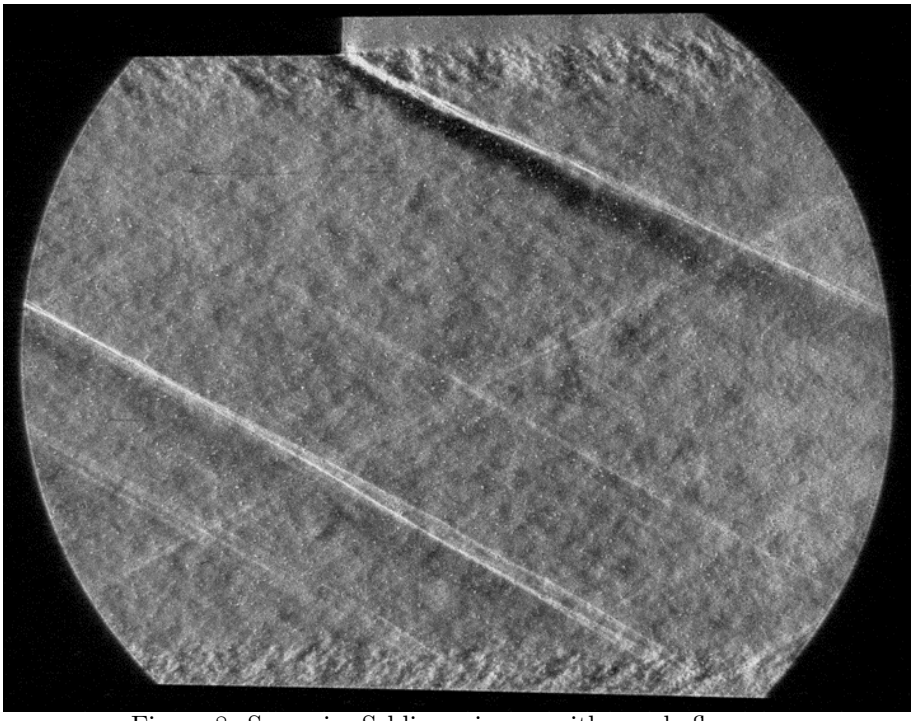
Figure 8: Spanwise Schlieren image with nozzle flow on.

determine convective velocities via optical methods. The Schlieren setup consisted of an LED light source, two 5-inch diameter telescopes, and a vertical knife edge. A picture of the Schlieren setup is shown in Fig. 7.

The spatial resolution of the Schlieren setup was 8,800 pixels/m. A representative frame of the Schlieren image with the cooling nozzle flow on is shown in Fig. 8. An incoming turbulent boundary, a boundary layer on the opposite wall, and the resulting mixing layer over the cavity can be clearly seen. A weak oblique shock is also formed at the corner of the step.

It is apparent that the boundary layer on the wall opposite the mixing layer is a potential contaminating effect on the wall-normal optical measurements. Previous analysis used a model for canonical boundary layers to determine

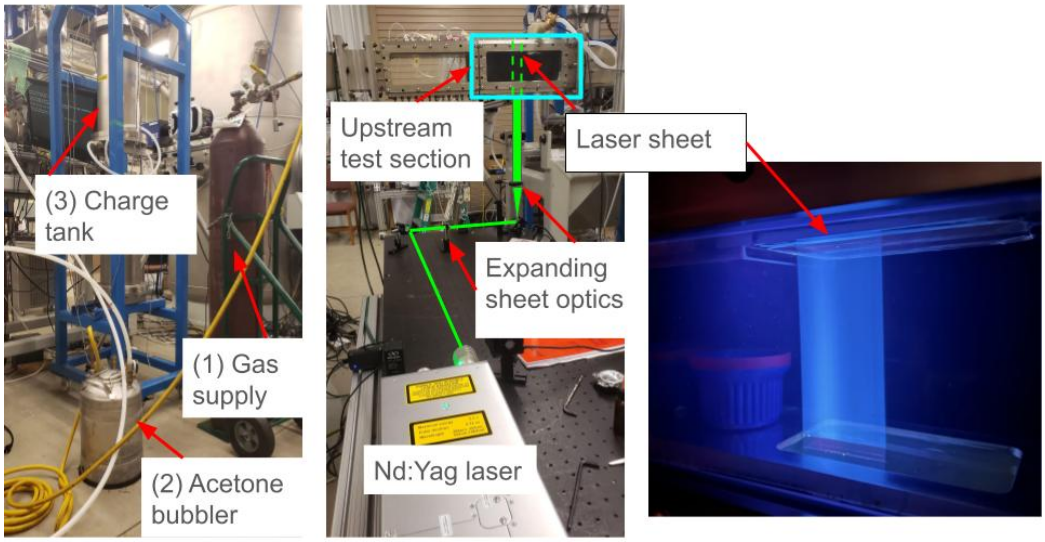

Figure 9: PLIF setup with optical and seeding elements labeled.

the level of additional distortion caused [5]. However, it is valuable to determine this quantity experimentally as well. In order to quantify and remove the aero-optical effects of the boundary layer on the opposite wall, additional Shack-Hartmann WFS measurements were taken, where the cooling jet test section insert was removed and replaced with an insert identical to the opposite insert. In this case, the laser beam propagated through two statistically-independent boundary layers on both sides of the test section. Later these tests will be refer to as the boundary layer measurements. Wavefront measurements were taken at the same 6 experimental stagnation temperatures, presented in Table 1, and the related aero-optical distortions due to the single boundary layer were calculated, as described in the next section.

2.3 PLIF

For Planar Laser-Induced Fluorescense (PLIF) measurements, laser excitation was produced by the 4th harmonic of an Nd:YaG laser with a 10 ns pulse width and a 100 Hz pulse rate, with a pulse energy of approximately 15 mJ per pulse. Sheet forming optics were used to produce a laser sheet with a wavelength of 266 nm, a width of 40 mm, and a thickness of approximately 150 μm at the sheet waist which is placed approximately 5 mm from the surface of the cavity. Two rounds of PLIF tests were performed with the beam at two downstream locations: one with the upstream edge of the sheet placed at the lip of the cavity, and one placed approximately 30 mm downstream of the first location. The sheet was placed at the center of the test section in all cases.

Seeding of the cooling nozzle flow was performed by bubbling the test gas through liquid acetone before filling the vessel supplying the cooling nozzle. For the air-air case, since pressurized oxygenated air combined with acetone is an unacceptable combustion risk, the test gas was substituted with pure nitrogen. Since nitrogen comprises approximately 78% of dry air and has comparable properties to dry air, it is a good substitute. For further analysis of this PLIF data, this case will continue to be referred to as the "air-air" case.

Recording of the laser sheet was performed by a Phantom v2512 High-Speed camera at a capture rate matched to the pulse rate of the laser. The signal of the acetone fluorescense was boosted by a LaVision Intensified Relay Optic (IRO). The camera was placed normal to the laser sheet. To minimize noise, the surfaces of the optical windows were thoroughly cleaned, and the test section insert opposite of the camera was coated in a graphite paint which minimizes reflection. A summary of the PLIF setup is shown in Fig. 9.

Since the pulse rate of the laser(and therefore the measuring frequency) is several orders of magnitude lower than the frame rate of the Schlieren and Shack-Hartmann measurements, it must be ensured that enough data is collected to satisfactorily converge both average and RMS values of intensity. From preliminary measurements,

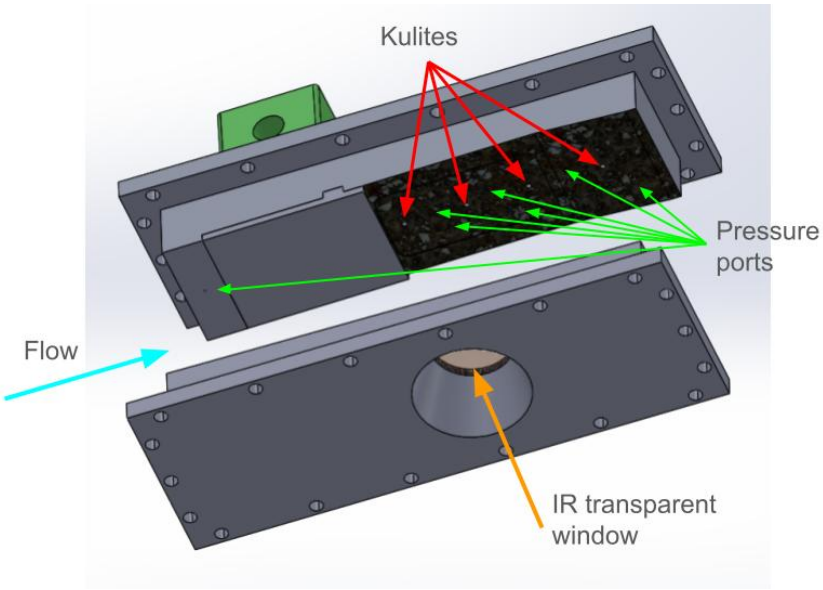

Figure 10: IR Thermography setup with components labeled.

it was determined that the nozzle valves should remain open for an elapsed time of 400 ms, including for the Helium-air case. This provides a total of approximately 35 frames, which was determined to be sufficient for proper analysis. PLIF measurements were done at freestream stagnation temperatures of 295K, 450K, and 650K, in order to match the conditions of the CFD simulations thus far performed.

2.4 IR Thermography

For Infrared (IR) Thermography, the glass insert in the test section insert was replaced with an aluminum piece of the same dimensions, whose flow-facing surface is finished with a black anodized process, such that has greater thermal emissivity. The remaining downstream surfaces of the test section insert were coated in a similar way. The test section insert opposite the nozzle insert has an infrared-transparent glass window mounted flush with the flow-facing surface of the insert, through which a thermal camera can capture thermal effects on the surface of the cavity which is under the effects of film cooling.

The IR camera used was the Optrix model Xi 400, which provides a temperature range of 0 $^{\circ}C$ - 250 $^{\circ}C$, among other ranges that may be selected from product software. It has an optical resolution of 382 x 288 pixels, a frame rate of 80 Hz, and a thermal sensitivity of 50 mK [4]. A summary of the IR Thermography setup can be found in Fig. 10. IR Thermography measurements were made at freestream stagnation temperatures of 295K, 500K, and 750K.

3. DATA REDUCTION APPROACHES

3.1 Aero-optical distortion levels

The Shack-Hartmann sensor measured deflection angles (θ_x, θ_z) at discrete locations (x, z) over the aperture. The deflection angles are related to the wavefront, $OPD(x, z, t)$, via the spatial gradient,$\theta_x = \partial OPD/\partial x, \theta_z = \partial OPD/\partial z$. In-house software was used to numerically integrate the measured deflection angles to obtain the wavefront time sequences over the aperture using Southwell's method [15]. To make the solution unique, the spatial mean value of the wavefront (piston component) was forced to zero at every time, $\int OPD(x, z, t)dxdz = 0$. In addition, the time-averaged wavefront (steady lensing) and instantaneous tip/tilt component were removed from each wavefront. Finally, the aperture-averaged levels of aero-optical distortion, OPD_{rms}, were calculated for different test conditions.

As noted before, the SHWFS laser bean must pass through both the mixing layer and the boundary layer on the opposite wall. Assuming the optical distortions from the contributing flows are statistically independent, the contributions to optical distortions may be described as [7]

$$OPD^2_{rms,total,ML-BL} = OPD^2_{rms,ML} + OPD^2_{rms,BL} \tag{1}$$

In case of the boundary layer measurements, where the laser beam passed through two boundary layers, aero-optical distortions from each boundary layer can be assumed to be the same. In this case, the levels of the aero-optical distortions from one boundary layer, $OPD_{rms,BL}$, can be computed from the total level of the distortions due to two boundary layers, $OPD_{rms,total,BL-BL}$, since

$$OPD^2_{rms,total,BL-BL} = OPD^2_{rms,BL1} + OPD^2_{rms,BL2} = 2 \cdot OPD^2_{rms,BL}$$

Therefore, to determine $OPD_{rms,ML}$ for the mixing layer alone,

$$OPD^2_{rms,ML} = OPD^2_{rms,total,ML-BL} - \frac{1}{2} OPD^2_{rms,total,BL-BL} \tag{2}$$

In addition, since the SHWFS aperture spans approximately the width of the test section, it will capture aero-optical effects from the side walls of the test section. To account for this, the spatial points comprising the area of the side-wall boundary layers were masked out before the wavefronts were calculated.

3.2 Heat Flux

IR Thermography measurements produce spatial maps of surface temperature. It was found that reflection from the optical window contaminated the data. To correct for this, the no-flow image was subtracted from the image. Assuming a constant initial surface temperature equal to the ambient temperature measured by lab sensors ($24.5°C$), the temperature map was then recalculated. No-flow subtracted temperature maps (taken from a snapshot with the cooling flow on) are shown in Fig. 11. Also shown are points of interest from which heat flux was extracted.

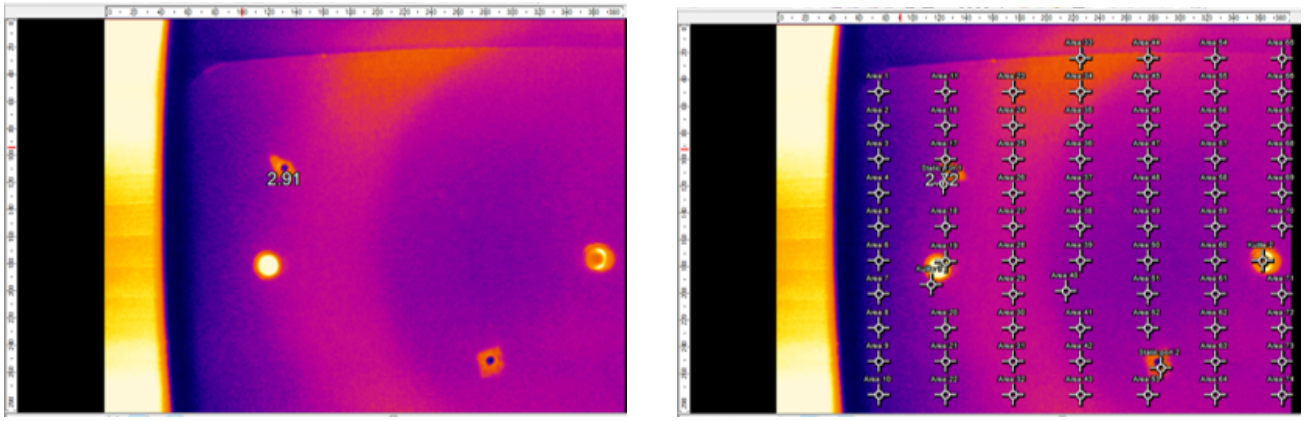

(a) (b)

Figure 11: Heat maps from IR Thermography (a) without labels and (b) with labels for instrumentation and points of interest.

Using the QCALC subroutine translated to MATLAB, heat flux can be extracted from a second-order approximation of the derivative of the temperature on the surface of the cavity [10].

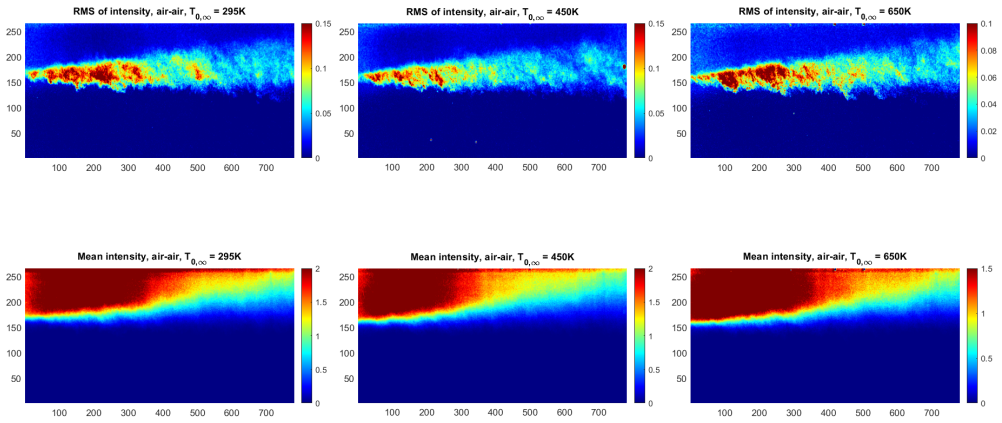

Figure 12: RMS and mean intensity, air-air. Colorbar axes denote intensity values. Other axes denote pixel numbers.

$$\frac{\partial T}{\partial t} = \alpha \frac{\partial^2 T}{\partial x^2} \tag{3}$$

Where α is thermal diffusivity. Discretized in time (subscript i) and space normal to the surface (subscript j),

$$\frac{T_{i+1,j} - T_{i,j}}{\Delta t} = \alpha \frac{T_{i,j+1} - 2T_{i,j} + T_{i,j-1}}{(\Delta x)^2}. \tag{4}$$

Beginning with a uniform initial temperature at $i = 1$, QCALC solves for $T_{i+1,j}$ using the measured surface temperature as one boundary condition, and back-face temperature (either assumed to be insulated or measured directly) as the other boundary condition. Following this, time-dependent heat flux at each surface location is calculated [2]. To ensure convergence for this explicit solution, a stability condition is applied to the Fourier number, F_0:

$$F_0 = \frac{\alpha \Delta t}{(\Delta x)^2} \ll \frac{1}{2}. \tag{5}$$

Previous tests of IR thermography have verified its level of accuracy. Using only the one-dimensional assumptions included in QCALC, experimental verifications produced a mean error of 8.9%. With correction for longitudinal heat transfer using an implicit solution, mean error decreased to 4.8% [13].

3.3 PLIF

The intensity of the laser sheet in the PLIF measurements cannot be assumed to be uniform. Therefore, a reference was taken by diffusing evaporated acetone through the test section. Test images were corrected by dividing out the intensity of this reference image. The mean-removed RMS and mean images with the jet flow on are presented in Figs. 12, 13, and 14.

Similarly to previous analysis of Schlieren images [6], the mean-removed RMS of intensity was analyzed at selected downstream locations, and the width at half-maximum taken as a parameter approximating the mixing layer thickness.

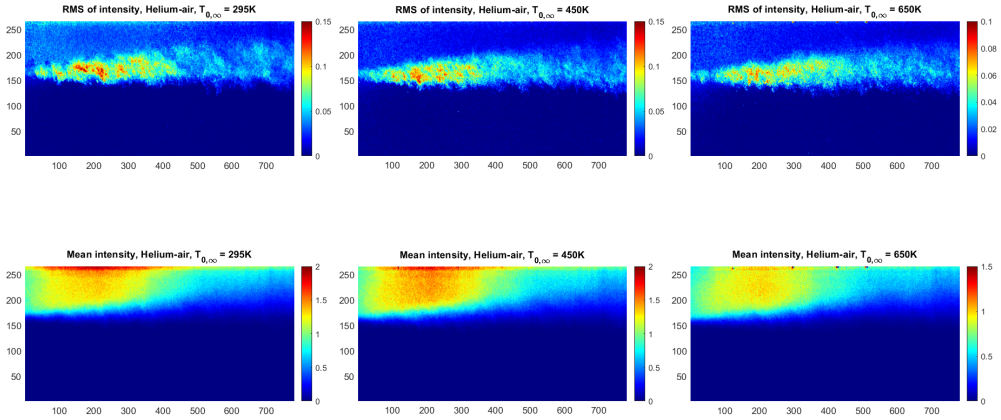

Figure 13: RMS and mean intensity, Helium-air. Colorbar axes denote intensity values. Other axes denote pixel numbers.

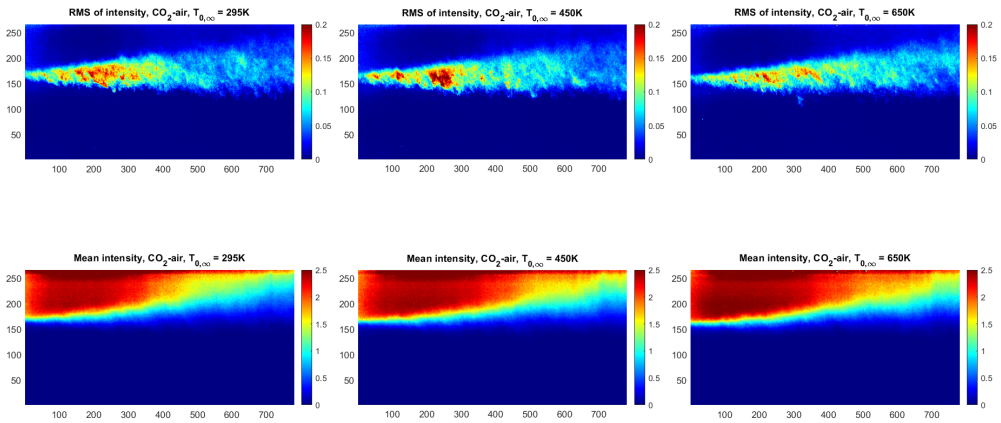

Figure 14: RMS and mean intensity, CO_2-air. Colorbar axes denote intensity values. Other axes denote pixel numbers.

4. RESULTS

4.1 Levels of Aero-Optical Distortions and Proposed Models

Relevant properties for the air-air, helium-air, and CO_2-air cases are listed in Tables 2, 3, and 4, respectively. As a reminder, the sub-indices "∞" and "*cool*" refer to the higher and lower velocity sides of the mixing layer, respectively.

Table 2: Flow properties, air-air.

$T_{0,\infty}$	295 K	350 K	450 K	550 K	650 K	750 K
$r = U_{cool}/U_\infty$	0.35	0.32	0.28	0.26	0.24	0.22
$s = \rho_{cool}/\rho_\infty$	0.59	0.70	0.90	1.1	1.3	1.5
U_c/U_∞	0.72	0.69	0.65	0.62	0.59	0.57
M_{cool}	0.54	0.54	0.54	0.54	0.54	0.54
M_C	0.56	0.62	0.70	0.76	0.81	0.86
$OPD_{rms,ML}$ (μm)	0.0286	0.0480	0.0372	0.0493	0.0490	0.0412

Table 3: Flow properties, helium-air.

$T_{0,\infty}$	295 K	350 K	450 K	550 K	650 K	750 K
$r = U_{cool}/U_\infty$	0.57	0.53	0.47	0.42	0.39	0.36
$s = \rho_{cool}/\rho_\infty$	0.078	0.093	0.12	0.15	0.17	0.20
U_c/U_∞	0.91	0.89	0.86	0.84	0.82	0.80
M_{cool}	0.30	0.30	0.30	0.30	0.30	0.30
$M_{C,\infty}$	0.19	0.22	0.27	0.32	0.36	0.39
$OPD_{rms,ML}$ (μm)	0.0606	0.0560	0.0580	0.0565	0.0504	0.0412

Table 4: Flow properties, CO_2-air.

$T_{0,\infty}$	295 K	350 K	450 K	550 K	650 K	750 K
$r = U_{cool}/U_\infty$	0.33	0.30	0.27	0.24	0.22	0.21
$s = \rho_{cool}/\rho_\infty$	0.85	1.0	1.3	1.6	1.9	2.2
U_c/U_∞	0.68	0.65	0.61	0.58	0.55	0.53
M_{cool}	0.65	0.65	0.65	0.65	0.65	0.65
$M_{C,\infty}$	0.64	0.70	0.78	0.85	0.90	0.94
$OPD_{rms,ML}$ (μm)	0.0551	0.0626	0.0575	0.0583	0.0552	0.0547

Here U_c is the isentropic approximation of the convective speed of the coherent structures in the mixing layer, which can be estimated as [12]

$$U_c = \frac{U_\infty + U_{cool}\sqrt{\frac{\rho_{cool}}{\rho_\infty}}}{1 + \sqrt{\frac{\rho_{cool}}{\rho_\infty}}}. \tag{6}$$

Note that Eq. 6 is also valid in case of dissimilar gases, when $\gamma_{cool} \neq \gamma_\infty$. Vales for U_c can be compared to those obtained from optical velocity analysis of the region of mixing, as described in previous work [6]. There is reasonable agreement between these values, as shown in Fig. 15.

The collected wavefronts were processed, as discussed before, and the results are provided in Tables 2 and 3 as well. Since these values were computed by subtracting generally large optical distortions of the boundary layer on the opposite wall from the overall distortions, the uncertainty of the measurements will be somewhat high. However, the numerical simulations of the mixing layer for $T_{0,\infty} = 295K$ gave the value of the aero-optical distortions of 0.03804 μm [3], which is in between the observed experimental results of 0.0286 μm for 295K and 0.0480 μm for 350K.

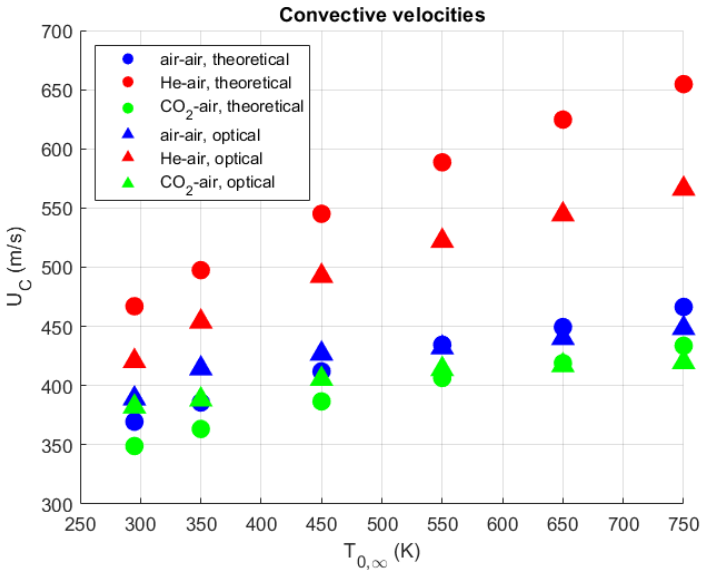

Figure 15: Values of convective velocity based on theoretical and optical velocity definitions.

4.1.1 Mixing-Driven Model

The obtained experimental results for all cases versus the subsonic model are presented in Fig. 16(a); clearly the model does not work at supersonic speeds. This is expected, as it was mentioned in the Introduction, that the existing model fails to work at supersonic speeds and also assumes that the total temperatures and gas species are the same on both sides of the shear layer. In the air-air case, the densities across the mixing layer were similar, see Table 2, and the density fluctuations are mostly due to pressure variations inside vortical structures. Previous analysis showed that a model based on this assumption produced a better scaling argument [6]. In the helium-air case, density on the cooling (helium) side are significantly lower than the density in the freestream, see Table 3. So, it is reasonable to assume that the density fluctuations are mostly due to mixing of light gas (helium) and heavy gas (air). If we ignore the pressure variations, the density variations will be due to velocity-dependent adiabatic cooling/heating. A similar mechanism is present in compressible turbulent boundary layers, allowing to develop useful aero-optical models [9, 8]. If pressure fluctuations are ignored, from the equation of state it follows that the density fluctuations are proportional to the temperature variations,

$$\frac{\rho_{rms}}{\rho_{ref}} = \frac{T_{rms}}{T_{ref}}.$$

In turn, a Strong Reynolds Analogy links the temperature and velocity fluctuations [14, 9],

$$C_P T_{rms} \sim U_{ref} u_{rms},$$

where U_{ref} is some reference speed. Combining the above equations, recognizing that for the mixing layers $u_{rms} \sim (U_\infty - U_{cool})$ [14], after some manipulations and using the same bulk-flow approach as previous [6], we get the following equation for the level of aero-optical distortions in predominantly mixing flows,

$$OPD_{rms} \sim K_{GD}\rho_{rms}\Lambda \sim K_{GD}\rho_{ref}\frac{U_{ref}(U_\infty - U_{cool})}{a^2_{ref}}\Lambda. \tag{7}$$

For the reference speed, we can use the convective speed value, $U_{ref} = U_C$. For the reference density and the square of the speed of of sound, we assume that they are a weighted linear combination of the corresponding quantities on both sides of the mixing layer,

$$\begin{aligned} \rho_{ref} &= \beta\rho_\infty + (1-\beta)\rho_{cool}, \\ a^2_{ref} &= \beta a^2_\infty + (1-\beta)a^2_{cool} \end{aligned} \tag{8}$$

where β is weighting parameter. Since density fluctuations are proportional to the local density, most of the contribution to the density variations are expected to be from heavy density (air) side of the mixing layer. Thus, β-parameter should be close to 1. After trial-and-error, it was found that $\beta = 0.85$ resulted in a very good agreement with the proposed mixing-dominant model. Likewise, for the CO_2-air case, contribution to the density variations are expected to be from the heavier (CO_2) side. Thus, β should be closer to 0 than to 1. It was found that $\beta = 0.35$ resulted in good agreement. For the air-air case, both sides should be equally weighted, making the parameter $\beta = 0.5$. As demonstrated in Fig. 16(b), the model produces a better linear scaling for the Helium-air and CO_2-air cases, although improvement for the air-air case is more questionable.

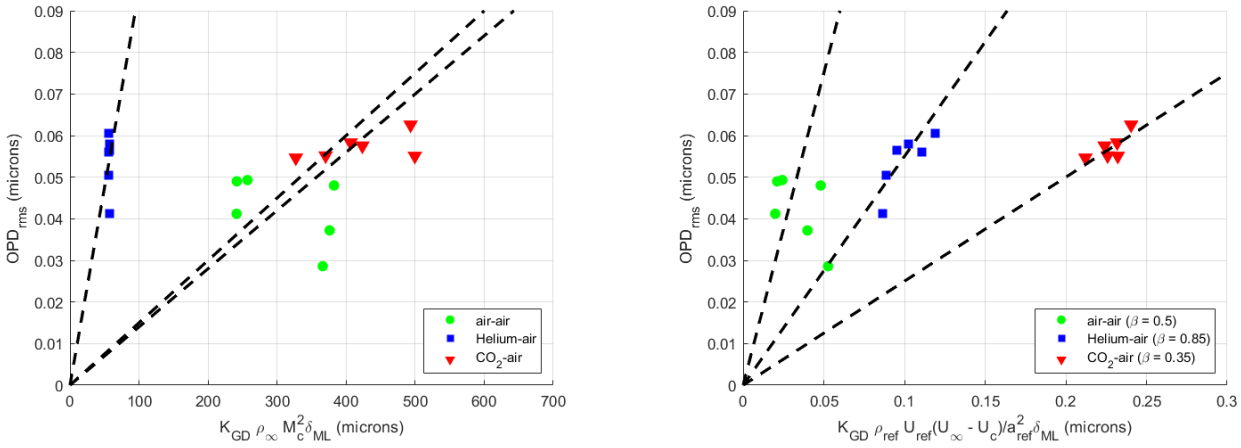

(a) (b)

Figure 16: OPD_{rms} from experiments versus (a) a subsonic model and (b) a new proposed mixing-dominant scaling, Eq. 7.

This model relies on the convective speed, U_C, Eq. 6. This equation was derived under the assumption of the low convective Mach number limit [12]. For presented results, the convective Mach numbers were in the range of 0.55 and 0.85 for the air-air case, between 0.12 and 0.26 for the helium-air case, and between 0.64 and 0.94 for the CO_2-air case. The convective Mach numbers for the air-air and CO_2-air cases might not considered to be low, possibly explaining the deviation of the air-air experimental data from the pressure-driven model in Fig. 16(b). So, the presented model should be considered as a preliminary model for low supersonic speeds only. The presented model should be used with caution in case of high supersonic and hypersonic freestream speeds, as the difference between the freestream and the cooling jet speeds, and the related convective Mach numbers become large. Also, the model uses the bulk-flow approach, which works for adiabatic wall boundary layers, but provided wrong predictions for boundary layers with non-adiabatic walls [8]. Future work will include the usage of the linking equation to develop the aero-optical models of the mixing layers, as this approach was demonstrated to develop a model which agreed much better with the experimental results for non-adiabatic wall boundary layers [8].

4.2 Spreading rates

For both PLIF and Schlieren measurements, width at half-maximum of the mean-removed RMS was taken as a parameter for mixing layer thickness. In all cases, the mixing layer demonstrated approximate linear growth as expected. Papamoschou and Roshko (1988) defined the growth rate of the "visual" mixing layer thickness without compressibility effects as

$$\delta_{vis,0} = 0.17 \frac{\Delta U}{U_C}. \tag{9}$$

The observed growth rates from PLIF and Schlieren were normalized by their respective values as defined above. This normalized growth rate is plotted against $M_{C,\infty}$ in Fig. 17. The decline in growth rate with convective

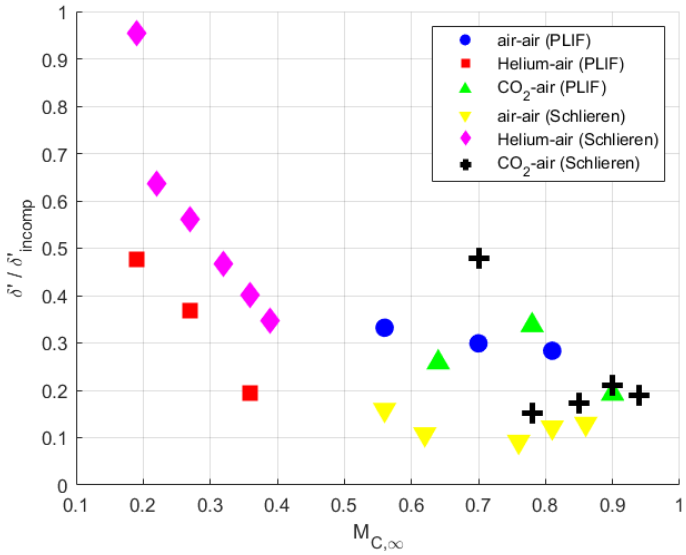

Figure 17: Observed growth rates normalized by incompressible values.

Mach number is consistent with previous analysis, as are the values of the normalized growth rate, which here as in Papamoschou and Roshko (1988) are shown to asymptote to approximately 0.2 [12]. Variation of the growth rate between identical conditions of PLIF and Schlieren measurements is high, however. It is likely that Schlieren measurements and PLIF measurements produce different growth rates when analyzed in the same way because of what aspect of the mixing layer each technique captures. Schlieren intensity is based on density variation, while PLIF intensity is nominally based on species concentration. Further examination of this discrepancy is needed.

4.3 Heat flux

Heat flux values, averaged over all points of interest, are shown in Fig. 18. It can be readily observed that, for the two higher stagnation temperatures, heat flux into the wall increases and remains constant with tunnel startup, and following cooling flow startup (at 0.4 s from tunnel startup), decreases.

To analyze the effectiveness of the cooling flow, the difference in heat flux into the wall between the period of time before the cooling flow was active and the period when it was active was analyzed. This parameter is plotted in Fig. 19 against the difference between the wall temperature (assumed constant at 300K), T_w, and the recovery temperature, T_r. It can be observed that selection of test gas makes little difference in the cooling effectiveness, and that there is a linear increase in the reduction of heat flux with increasing temperature disparity.

5. CONCLUSIONS

Optical measurements of a total temperature-mixmatched and species-mismatched supersonic mixing layer were made using time-resolved Shack-Hartmann WFS, Schlieren photography, and PLIF measurement techniques. The mixing layer was created by a two-dimensional jet blown through a backward-facing step with a depth of $5mm$. Using air as a test gas, the jet exit Mach number was $M \approx 0.53$. With helium as a test gas, the jet exit Mach number was $M \approx 0.30$. Using CO_2 as a test gas, the jet exit Mach number was $M \approx 0.65$. The jet was placed at the wall of a $M = 2$ wind tunnel and connected to an external gas supply to match the static pressure in the test section. Spanwise Schlieren measurements in the spanwise direction over an area with a diameter of 125 mm were made at sampling frequencies of 25 kHz and 100 kHz. Wall-normal Shack-Hartmann WFS measurements in the direction normal to the mixing layer with a beam diameter of 50 mm were performed, with the edge of the beam set 15 mm downstream of the cooling nozzle exit. Wind tunnel total temperature

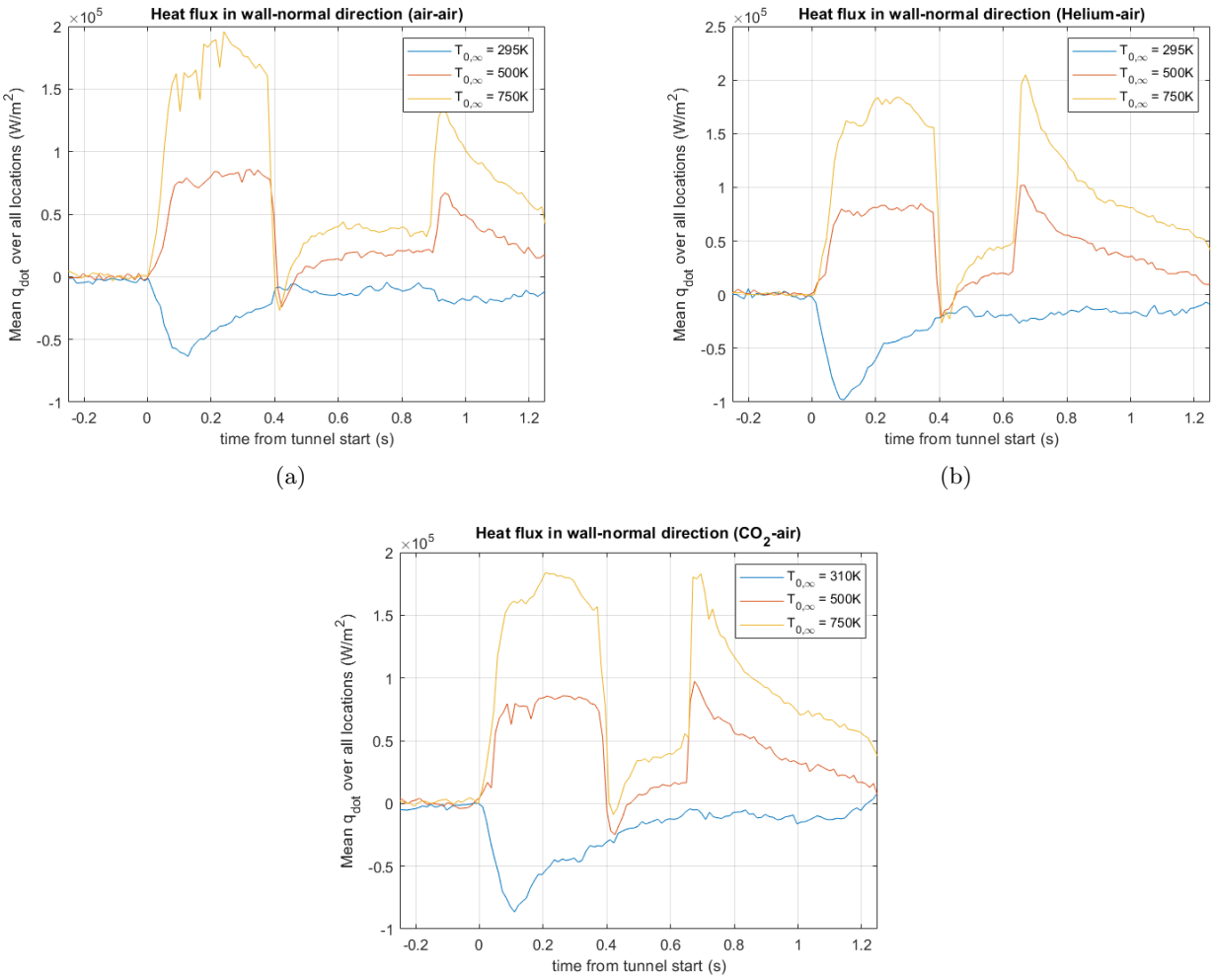

(a) (b)

(c)

Figure 18: Spatially averaged heat flux, (a) air-air, (b) Helium-air, (c) CO_2-air.

was varied between $295K$ and $750K$. PLIF measurements were taken using a sheet 40 mm in length, captured at the same rate as a 100 Hz pulsed laser.

Flow parameters including jet exit velocity and convective velocity were extracted from Schlieren measurements using optical velocity techniques. Time-averaged levels of aero-optical distortions, expressed as OPD_{rms} values, were extracted from Shack-Hartmann WFS data. A scaling model was developed based on density fluctuations caused by the mixing of two gases with highly dissimilar densities. For the Helium-air and CO_2-air cases, the proposed models provide a better agreement to the experimental data than the subsonic model developed for shear layers. While the subsonic model also does not provide a good prediction for the air-air case, the proposed model appears less effective for this case specifically. The model can be used to predict aero-optical distortions caused by cooling flow over optical windows on supersonic vehicles.

Future work will include thorough analysis of the results of PLIF measurements. The wall-normal profiles of fractional species concentration provided by PLIF, corrected by velocity profiles provided by concurrent computational experiments [3] will produce profiles of density and density fluctuation. These profiles may be substituted into the Linking Equation,

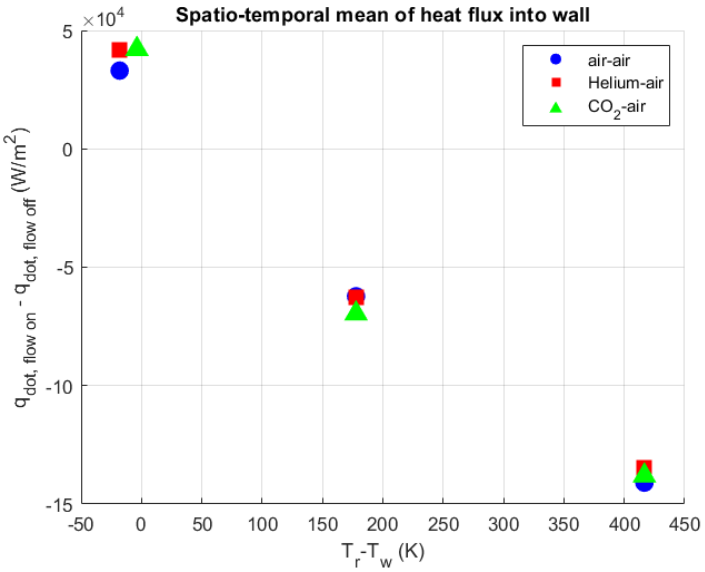

Figure 19: Difference in spatio-temporally averaged heat flux between cooling-flow-on and cooling-flow-off cases.

$$OPD_{rms}^2 = 2K_{GD}^2 \int_0^L \rho_{rms}^2(y)\Lambda(y)dy. \tag{10}$$

This approach will serve to produce a unified model for all three test gas cases [7]. Subsequent analysis techniques and modelling efforts will assist in the design of cooled windows such that sufficient cooling is balanced with minimized aero-optical distortions.

Acknowledgements

This work is supported by the Office of Naval Research, Grant number N00014-22-1-2454 with Dr. Eric Marineau serving as program manager. The U.S. Government is authorized to reproduce and distribute reprints for governmental purposes notwithstanding any copyright notation thereon.

The authors also would like to thank Philip Lax for his assistance setting up the experiments and operating the tunnel, as well as Luke Ricci for his assistance in the setup and analysis of PLIF experiments.

References

[1] Philip Andrews et al. "Flow Characterization at Heated Air Supersonic Facility SBR-50". In: *Fluids* 7.5 (2022). ISSN: 2311-5521. DOI: 10.3390/fluids7050168. URL: https://www.mdpi.com/2311-5521/7/5/168.

[2] C. F. Boyd and A. Howell. *Numerical investigation of one-dimensional heat-flux calculations*. Oct. 1994.

[3] P Castillo et al. "Wall-Modeled Large-Eddy Simulation of Supersonic Mixing Layer for Aero-Optical Distortion Analysis". In: *AIAA Paper 2024-2516* (2024).

[4] *Compact spot finder IR camera*. Xi 400. Optris Infrared Measurements. Feb. 2024.

[5] Aaron Fassler, Sergey Leonov, and Stanislav Gordeyev. "Optical effects of a temperature-mismatched supersonic mixing layer". In: *Unconventional Imaging, Sensing, and Adaptive Optics 2023*. Ed. by Jean J. Dolne, Mark F. Spencer, and Santasri R. Bose-Pillai. Vol. 12693. International Society for Optics and Photonics. SPIE, 2023, p. 1269316. DOI: 10.1117/12.2677429. URL: https://doi.org/10.1117/12.2677429.

[6] Aaron Fassler, Sergey B. Leonov, and Stanislav Gordeyev. "Aero-Optical Effects of a Species-Mismatched Supersonic Mixing Layers". In: *AIAA SCITECH 2024 Forum*. DOI: 10.2514/6.2024-1027. eprint: https://arc.aiaa.org/doi/pdf/10.2514/6.2024-1027. URL: https://arc.aiaa.org/doi/abs/10.2514/6.2024-1027.

[7] S. Gordeyev, E.J. Jumper, and M.R. Whiteley. *Aero-Optical Effects: Physics, Analysis and Mitigation*. Wiley Series in Pure and Applied Optics. Wiley, 2023. ISBN: 9781119037170. URL: https://books.google.com/books?id=hqujEAAAQBAJ.

[8] Stanislav Gordeyev et al. "Aero-optical measurements in a subsonic, turbulent boundary layer with non-adiabatic walls". In: *Physics of Fluids* 27.4 (Apr. 2015), p. 045110. ISSN: 1070-6631. DOI: 10.1063/1.4919331. URL: https://doi.org/10.1063/1.4919331.

[9] Stanislav Gordeyev et al. "Experimental studies of aero-optical properties of subsonic turbulent boundary layers". In: *Journal of Fluid Mechanics* 740 (2014), pp. 214–253. DOI: 10.1017/jfm.2013.658.

[10] Thomas J. Juliano, Laura A. Paquin, and Matthew P. Borg. "HIFiRE-5 Boundary-Layer Transition Measured in a Mach-6 Quiet Tunnel with Infrared Thermography". In: *AIAA Journal* 57.5 (2019), pp. 2001–2010. DOI: 10.2514/1.J056750. eprint: https://doi.org/10.2514/1.J056750. URL: https://doi.org/10.2514/1.J056750.

[11] Chun-Chi Li, Yi-Chan Lin, and M. Hsieh. "3-D Simulation of external cooling of aero-optical side window". In: *2011 IEEE 3rd International Conference on Communication Software and Networks* (2011), pp. 214–218.

[12] Dimitri Papamoschou and Anatol Roshko. "The compressible turbulent shear layer: an experimental study". In: *Journal of Fluid Mechanics* 197 (1988), pp. 453–477. DOI: 10.1017/S0022112088003325.

[13] Jens Rataczak, Carson Running, and Thomas Juliano. "Verification of quantitative infrared thermography heat-flux measurements". In: *Experimental Thermal and Fluid Science (EXP THERM FLUID SCI)* 121 (Feb. 2021), p. 110274. DOI: 10.1016/j.expthermflusci.2020.110274.

[14] A.J. Smits and J.P. Dussauge. *Turbulent Shear Layers in Supersonic Flow*. Springer New York, 2006. ISBN: 9780387263052. URL: https://books.google.com/books?id=KtpFdcTEbQQC.

[15] W. H. Southwell. "Wave-front estimation from wave-front slope measurements". In: *Journal of the Optical Society of America (1917-1983)* 7.8 (Aug. 1980), p. 998.

[16] ALLEN SPENCER and WILLIAM MOORE. "Design trade-offs for homing missiles". In: *Annual Interceptor Technology Conference*. DOI: 10.2514/6.1992-2755. eprint: https://arc.aiaa.org/doi/pdf/10.2514/6.1992-2755. URL: https://arc.aiaa.org/doi/abs/10.2514/6.1992-2755.